

# Sheared Thick-Film Electrode Materials Containing Silver Powders with Nanoscale Surface Asperities Improve Solar Cell Performance

Mohamed M. Hilali,\* Shweta Pal, Rishabh V. More, Rebecca Saive, and Arezoo M. Ardekani


Thick-film screen-printed fine-line metallization is one of the most important process steps in the whole production chain of photovoltaic cell manufacturing as variations in industrial solar cell performance mainly depend on electrode properties. The impact of Ag powder surface topography on viscoelastic characteristics and geometry of solar cell electrodes is studied. Numerical simulations for concentrated non-Brownian suspensions show that shear viscosity and storage modulus increase with particle roughness. Experimental rheological analysis shows improvement in thixotropy and shear storage modulus for pseudoplastic electrode materials with corrugated Ag powders. Consequently, viscoelastic recovery is enhanced for frontside electrode gridlines with rough-surface Ag powders. This results in aspect-ratio and cross-sectional symmetry enhancement for rough-surface Ag powder gridlines compared with smooth-surface Ag powder gridlines. Rough-surface Ag powder gridlines have smaller height variations, making them more suitable for high-throughput screen printing. Optical simulations show improved light redirection into the solar cell for gridlines formed from rough-surface Ag powders, leading to higher solar cell photocurrent. The improved gridline definition results in an increase in short-circuit current density, yielding average efficiency improvement of  $\approx 0.1\%$  absolute for monocrystalline-Si solar cells with screen-printed gridlines having rough-surface Ag powders. This results in monocrystalline-Si solar cells with 22.45% average conversion efficiency.

## 1. Introduction

The overwhelming majority of high-efficiency crystalline-Si (c-Si) solar cells remain the most commercially feasible option for photovoltaic (PV) energy generation dominating the industry with more than 90% market share. These solar cells have optimized frontside Ag electrode metallization with fine gridlines, which are currently less than  $40\ \mu\text{m}$  in width.<sup>[1]</sup> Screen printing is the dominant process for applying electrode metallization to c-Si solar cells. There are several reasons for this; these include the ability of the screen printing process to achieve high-throughput metallization, the ease of scalability of this process in production lines, good reliability, and the relative simplicity of the setup, all of which make it an economically advantageous process technology that is the preferred technique for solar cell contact metallization in large-volume manufacturing. In addition, screen printing is not an environmentally harmful process technology, and it is resource-efficient with minimal waste material.

For solar cell contact grid metallization, it has been previously shown that mesoscale metallic front contacts outperform nanoscale contacts in enhancing the optical absorption within the silicon.<sup>[2]</sup> This provides a positive outlook for the

M. M. Hilali  
Department of Materials and Physics  
Ganjiang Innovation Academy  
Chinese Academy of Sciences  
Jiangxi 341000, P. R. China  
E-mail: MHilali@pharos-zj.com, MHilali@gia.cas.cn

 The ORCID identification number(s) for the author(s) of this article can be found under <https://doi.org/10.1002/aesr.202100145>.

© 2021 The Authors. Advanced Energy and Sustainability Research published by Wiley-VCH GmbH. This is an open access article under the terms of the Creative Commons Attribution License, which permits use, distribution and reproduction in any medium, provided the original work is properly cited.

DOI: 10.1002/aesr.202100145

M. M. Hilali  
Research and Development  
Pharos Materials  
Inc.  
6920 Santa Teresa Blvd., Suite 103, San Jose, CA 95119, USA

S. Pal, R. Saive  
MESA+ Institute for Nanotechnology  
Inorganic Materials Science (IMS)  
University of Twente  
Enschede 7500 AE, The Netherlands

R. V. More, A. M. Ardekani  
School of Mechanical Engineering  
Purdue University  
West Lafayette, IN 47907, USA

prospects of printed frontside grid metallization technology used for mass production of industrial solar cells to further improve the solar cell photocurrent and conversion efficiency. Over the past two decades economies of scale had an increased impact on solar cell cost reduction, becoming as effective as research and development in lowering the cost of PV modules.<sup>[3,4]</sup> Logistically, increasing volume or throughput is critical for reducing cost per manufacturing unit as much as possible. Therefore, reducing cycle time and raising production throughput of the screen printing process is a major goal for industrial solar cell manufacturers. The current single-lane screen print throughput in the PV industry is quite high—around 3500 wafers per hour for passivated-emitter rear-contact (PERC) solar cells<sup>[5]</sup>; these production speeds are expected to increase further over this decade.<sup>[1]</sup> Hence, utilizing electrode pastes that can be screen-printed (SP) well at high print-speeds of 500–600 mm s<sup>-1</sup> required by the PV industry is especially important.

The typical solar cell frontside Ag electrode paste material is composed of Ag particles constituting the functional phase, glass particles or frit acting as a high-temperature binder, and the organic medium or vehicle, which acts as the carrier phase that is generally composed of organic solvents, resins, as well as suitable rheological additives.<sup>[6,7]</sup> The sintered Ag powders in the paste allow for frontside electrode grid conductivity, solderability, and they play a critical role in the Ag–Si interface contact formation as well.<sup>[8]</sup> In addition to providing adhesion to the Si wafer after contact metallization firing, the glass frit is necessary for etching through the antireflective coating and passivating layer during contact firing allowing for high-quality Ag–Si contacts with low contact-resistivity to be formed.<sup>[8]</sup> The Ag powders are typically suspended in a mixed solution of nonvolatile polymeric binder resins, organic solvents, as well as thixotropic agents, and surfactants to control the viscoelastic and shear-thinning flow behavior of the pseudoplastic electrode material (Ag paste) and to provide the necessary cohesiveness and substrate adhesion for the wet-printed and dried electrode material.<sup>[9–12]</sup> During the contact-firing step, all organic constituents of the paste are burned out.

The pseudoplastic flow characteristics of SP Ag pastes and concepts related to shear-thinning behavior and yield stress control via organic constituents of the paste have been previously investigated in different experimental studies.<sup>[11–14]</sup> As the Ag paste is first significantly sheared during the screen printing process so that it can be transferred through the small openings of the screen mesh, there are some critical paste rheological properties that are required to make this possible.<sup>[15]</sup> Ag pastes for frontside PERC Si solar cells currently in large-volume production are high concentration suspensions of spherical Ag powders that account for more than 85% by weight of the paste with a particle-size distribution D<sub>50</sub> diameter that is less than 5 μm.<sup>[16,17]</sup> Ag pastes exhibit non-Newtonian fluid behavior with significant pseudoplastic shear-thinning following a noticeable characteristic yield stress.<sup>[18,19]</sup> In addition, thixotropic behavior (time-dependent zero-shear viscosity recovery) is crucial for SP Ag pastes to achieve well-defined lines as it prevents arbitrary transition from a solid to a fluid form.<sup>[20,21]</sup>

In particular, the frontside Ag electrode material plays a crucial role in industrial high-volume production and performance of c-Si PV cells. For PV cells in industrial production, it is

required that the frontside gridline height is increased as much as possible while simultaneously reducing the gridline width—that is the gridline aspect-ratio (AR) needs to be maximized.<sup>[1]</sup> The frontside Si solar cell electrode metallization via Ag paste screen printing technology has been remarkably successful with significant advancements over the past couple of decades; the printed electrodes resulted in improved solar cell performance over the years due to the decrease in contact resistivity and increase in line-conductivity, as well as reduced electrode gridline width. In industry, electrode gridlines have decreased from about 100–120 μm in 2006<sup>[22]</sup> to current values of around 35 μm.<sup>[1]</sup> Moreover, in recent lab research studies gridlines with 20 μm width<sup>[23]</sup> and 0.95 AR have been achieved.<sup>[24,25]</sup>

There are different aspects of the flatbed printing technology that can be improved to help achieve the goal of reduced gridline width and higher ARs; these include the screen design or architecture,<sup>[26]</sup> screen emulsion properties,<sup>[25]</sup> and the paste constituents and rheology behavior.<sup>[6,27–30]</sup> This study is concerned with the latter. The trend of gridline width reduction over the past 16 years was primarily driven by Ag electrode paste optimization; more recently, the screen has been independently optimized to allow for printing through narrower finger openings. Using dynamic oscillatory rheometry, Hoornstra et al. characterized the rheological behavior and thixotropic recovery characteristics of various Ag pastes.<sup>[18]</sup> Nonetheless, these characterization results were not correlated to the printed electrode geometric properties. During the past 5 years, the effects of Ag powder morphologies and sizes on the mechanical, rheological, and electrical properties of SP Ag pastes for silicon solar cells have been investigated to some degree.<sup>[27]</sup> The influence of the electrode paste material rheology on the ability of the screen printing process to print high-performing fine-line-definition for frontside solar cell metallization grid has been previously discussed.<sup>[14,28]</sup> Rheological parameters of solar cell frontside electrode Ag paste materials were also related to the SP finger geometry, demonstrating the importance of yield stress and complex shear modulus ( $G^*$ ).<sup>[28]</sup> Also, the impact of the elastic component (storage modulus) of  $G^*$  on the AR of the printed frontside solar cell metallization gridlines was previously illustrated for paste-dispensing technology.<sup>[31]</sup> By appropriately formulating the organic vehicle of the Ag electrode paste, wall slip at the emulsion surface was shown to substantially enhance paste transfer through the screen mesh.<sup>[30]</sup> And, by investigating various screen emulsion coatings, enhanced wall-slip behavior of commercial Ag pastes was demonstrated to enable fine-line screen printing of solar cell gridlines.<sup>[32]</sup> In addition to the influence of the solar cell frontside electrode metallization paste's rheological behavior, the screen mesh design is important to allow suitable Ag pastes to reach their optimal performance.<sup>[29]</sup>

The Ag powder is the main constituent of the solar cell frontside metallization paste in both wt% and vol%. Thus, the Ag powder is expected to have a crucial role in the rheological and electrical performance of the thick-film frontside metallization grid. The effect of the Ag powder on the SP metallization sintering characteristics and contact formation mechanism has been previously studied extensively—models explaining the contact formation process during firing and related optimizations have been proposed.<sup>[33–36]</sup> It was previously suggested by Lin et al. that the surface property of the filler powder is a critical controlling

factor for the rheological behavior of SP pastes.<sup>[13]</sup> However, we have not found any previous study on the effect of the surface topography of inorganic constituents in the printed thick-film material on the viscoelastic behavior, AR, and related optical redirection of printed solar cell gridlines. In this article, we study the effect of the surface topography of Ag powders in the SP thick-film electrodes on the rheological and viscoelastic behavior of the pseudoplastic electrode paste material, and the resulting optical and electrical performance is analyzed. Rheological behavior of the metallization pastes is explained based on numerical simulations and experimental characterization. We also assess the effects of the different electrode paste materials on print quality. In addition, gridline-definition analysis and optical simulations are used to explain the related optical effects on the solar cell photocurrent due to the different gridline geometries. The main goal of this work is to ultimately improve the solar cell photocurrent and overall performance as well as to demonstrate new paths that may lead to enhancements in the quality of the thick-film solar cell metallization at higher print-speeds.

## 2. Results and Discussion

### 2.1. Effect of Silver Powder Topography on the Shear-Thinning Behavior of the Pseudoplastic Electrode Materials

Substantial shear-thinning to lower the viscosity at high shear-rates is a necessary characteristic for the frontside grid metallization pseudoplastic Ag paste to flow through fine mesh-openings, whereby it experiences high shear-rates. The tangential velocity gradient known as the shear-rate is given by

$$\dot{\gamma} = \frac{dv}{dy} \approx \frac{\text{squeegee speed}}{\text{grid - pattern screen mesh opening width}} \quad (1)$$

And the viscosity,  $\eta(\dot{\gamma})$ , and shear stress,  $\tau(\dot{\gamma})$ , shear-thinning behavior of the SP metal paste may be approximated by the Ostwald-de Waele's power-law

$$\eta(\dot{\gamma}) = c \cdot \dot{\gamma}^{p-1} \quad \text{and} \quad \tau(\dot{\gamma}) = c \cdot \dot{\gamma}^p \quad (2)$$

where  $c$  is the flow-consistency index and the flow-behavior power index  $p < 1$  for shear-thinning. The shear-rate of the SP solar cell electrode Ag paste material is extremely high,

$>10\,000\,1/s$ , as it flows through the screen grid-pattern mesh opening. The Ag powder concentration in the frontside solar cell electrode metallization pastes is typically  $\approx 50\%$  by volume, or slightly higher. On the other hand, the glass powder concentration by volume in these pastes is  $\approx 20$  times less than that of the Ag powder. Hence, we consider the Ag powder as the key solid filler material that affects the performance of the paste rheology. This can be understood based on the effect of particle concentration on relative viscosity, which can be estimated by the following model<sup>[37]</sup>

$$\eta_r = \left(1 - \frac{\phi}{\phi_m}\right)^{-2} \quad (3)$$

where  $\eta_r$  is the relative viscosity;  $\phi$  and  $\phi_m$  are the volume fraction and the maximum packing volume fraction of the dispersed particles, respectively. The viscosity of the SP pseudoplastic paste is the key parameter that strongly affects the gridline-resolution and print quality.<sup>[38]</sup> It is typically true that more viscous pastes result in finer SP gridlines.<sup>[39]</sup>

The scanning electron microscopy (SEM) micrograph images of the two silver powders used for this study are displayed in **Figure 1**. The smooth and corrugated Ag powder distributions have close SSA values because of the higher volume percentage of finer particles for the smooth-surface Ag powder distribution compared with the corrugated-surface Ag powder distribution as shown by the particle-size distribution plots in **Figure 2**. It is observed that for all three groups of pastes for which rheological analysis was performed the Ag paste shear viscosity increases when going from smooth Ag powder paste to corrugated Ag powder paste as shown in **Figure 3**.

For zero-shear behavior, the measured yield stress is evaluated for the different Ag paste groups with corrugated and smooth Ag powders, as illustrated in **Figure 4**. For lower viscosity group A Ag pastes, the yield stress (see **Figure 4a**) is quite close for both corrugated and smooth Ag powder pastes,  $\approx 48.5$  and  $50$  Pa, for the former and latter, respectively. For group B Ag pastes, the yield stress is somewhat similar,  $\approx 56$  and  $\approx 57$  Pa, for smooth and corrugated Ag powder pastes (see **Figure 4b**), respectively; and for group C Ag pastes, the yield stress is  $\approx 50$  and  $55$  Pa, for smooth and corrugated Ag powder pastes, respectively (see **Figure 4c**). The most apparent difference in rheological behavior between pastes formulated with rough-surface Ag powders and

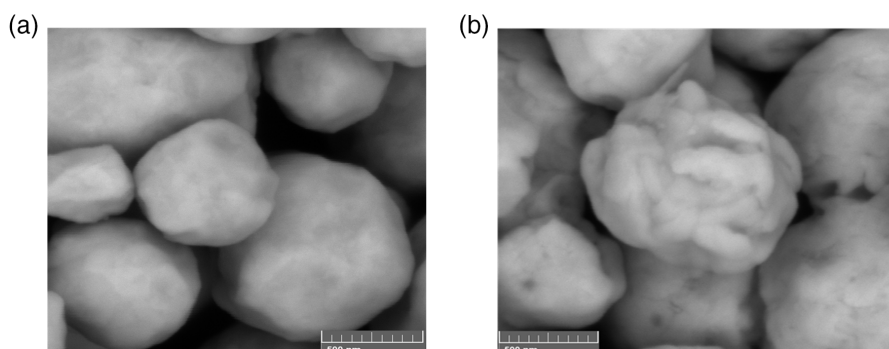


**Figure 1.** SEM micrographs of Ag powder with a) smooth-surface topography, and b) corrugated-surface topography. The scale shown in the micrographs is 500 nm.

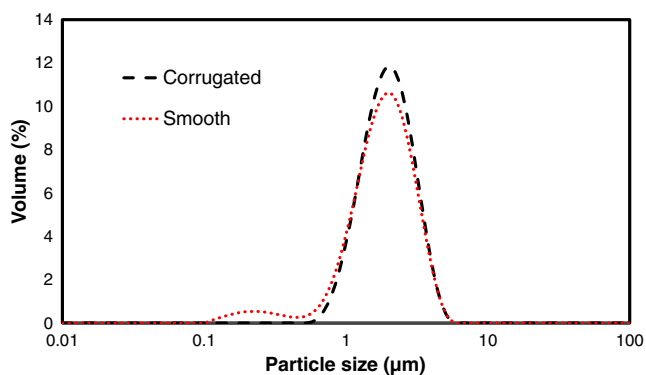


**Figure 2.** Particle-size distribution plots for corrugated- and smooth-surface Ag powders.

those formulated with smooth-surface Ag powders is mainly exhibited at higher shear-rates.

Higher viscosity pseudoplastic metal powder materials can achieve higher gridline ARs; however, typically the gridline print quality (low SP gridline discontinuities) will not be as good as that of pseudoplastic metal powder materials of lower viscosity for the same screen finger openings and print-speed. Previously, we had illustrated this phenomenon, showing that higher viscosity solar cell electrode materials will yield more defects, particularly for narrower screen finger openings and for higher print-speeds.<sup>[40]</sup> Therefore, our approach here to improve line definition differs from the concept of Xu et al.<sup>[30]</sup> in that we make use of the shear modulus behavior at high shear-rates to improve gridline AR rather than further increasing

the yield stress and viscosity of the printed electrode material. This should help minimize the likelihood of increasing print defects for the fine-line high shear-rate screen printing process. As shown in **Figure 5**, rougher Ag powder surface improves the degree of thixotropy: it is improved  $\approx 1.4$  times for group A Ag paste, A-c, and it is almost doubled for group B Ag paste, B-c. The area of the shear stress hysteresis loop for the different pastes studied is quantified in **Table 1**. In general, the Ag powder surface asperities seem to increase the degree of thixotropy of the pseudoplastic electrode materials as shown in **Figure 5a,b**. For group C pastes, for which the smooth Ag powder paste already had a relatively high viscosity and thixotropic index, the degree of thixotropy remains very similar for the corrugated Ag powder and smooth Ag powder pastes (see **Figure 5c** and **Table 1**). Comparing the area of shear stress versus shear-rate hysteresis loop, the increase in thixotropy due to Ag powder roughness is greater for the paste with intermediate thixotropic index and viscosity as shown in **Figure 5b** and **Table 1**.

## 2.2. Numerical Analysis

In this section, we numerically model a dense non-Brownian suspension in a Newtonian fluid under a simple shear flow to study the effect of particle roughness in a concentrated particle suspension. The goal is to better understand the effect of the Ag powder topography on the rheological behavior of the SP Ag pastes. To achieve this, we model the hydrodynamic interactions using the Ball–Melrose approximation<sup>[41]</sup> to Stokesian Dynamics<sup>[42]</sup> and utilize a discrete element modeling (DEM) approach to model the related effects due to the presence of asperities on the surface of the particles. The particle Reynolds numbers

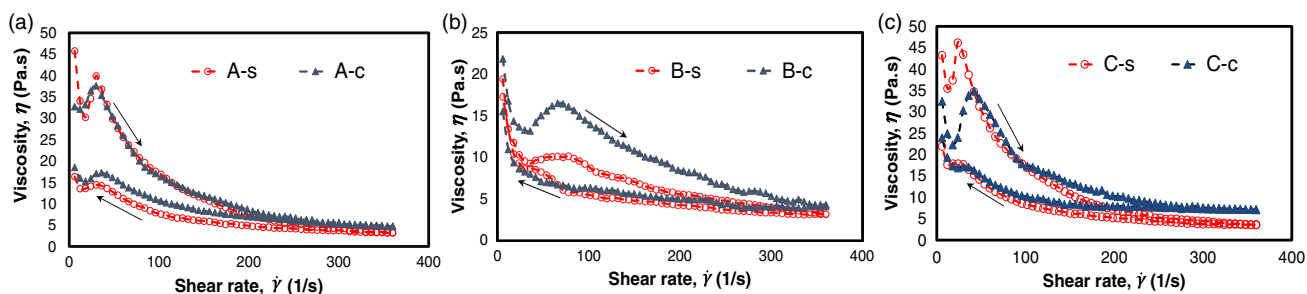


**Figure 3.** Viscosity versus shear-rate plots for smooth and corrugated Ag powders for pseudoplastic Ag electrode paste groups a) A, b) B, and c) C. The arrows indicate increasing and decreasing shear-rates. Part (c): Adapted with permission.<sup>[40]</sup> Copyright 2018, IEEE.

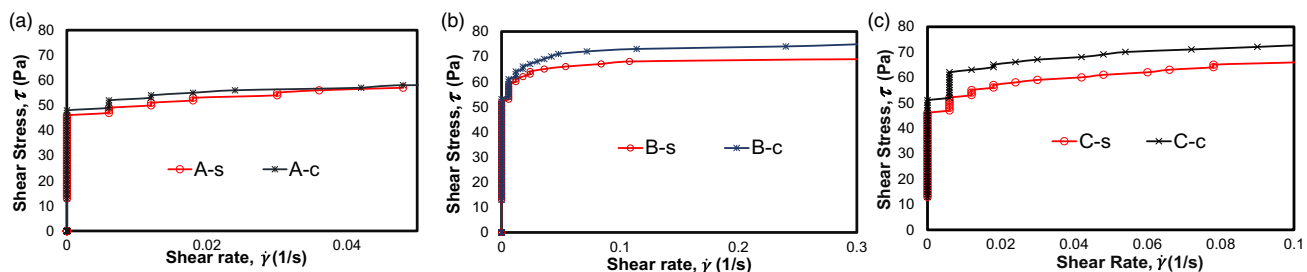


**Figure 4.** Yield stress point evaluated from shear stress versus shear-rate plots for smooth and corrugated Ag powders for pseudoplastic Ag electrode paste groups a) A, b) B, and c) C. The yield stress measurement was conducted as explained in the Experimental Section.

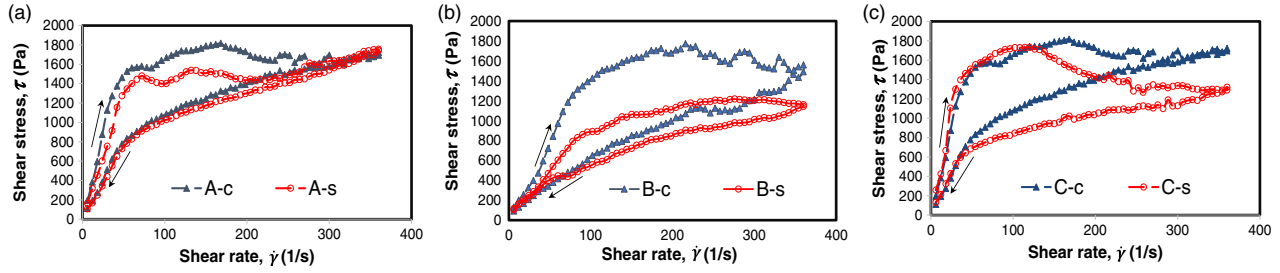


**Figure 5.** Shear stress versus shear-rate plots for smooth and corrugated Ag powders for pseudoplastic Ag electrode paste groups a) A, b) B, and c) C. The arrows indicate increasing and decreasing shear-rates. Part (c): Adapted with permission.<sup>[40]</sup> Copyright 2018, IEEE.

**Table 1.** Measured viscosity (at 25 °C and 10 rpm) and area of the hysteresis loop for the different pastes studied.

| Ag pastes | Viscosity (Pa.s) | Area of hysteresis loop (Pa/s) |
|-----------|------------------|--------------------------------|
| A-s       | 187              | 82 761                         |
| A-c       | 193              | 116 598                        |
| B-s       | 238              | 139 668                        |
| B-c       | 267              | 284 125                        |
| C-s       | 266              | 180 868                        |
| C-c       | 259              | 181 141                        |

are negligible owing to their small sizes. Hence, this system follows a Stokes flow regime, and velocities of the particles have linear dependence on the hydrodynamics forces acting on the particles. We briefly describe the methodology here. A detailed discussion on the numerical tool and its validation can be found elsewhere.<sup>[43–46]</sup> Starting from the equations of motion and calculating the hydrodynamic forces; for a Stokes flow regime, the force balance of particles after neglecting inertia can be described by the following equation

$$0 = \begin{pmatrix} F_H \\ T_H \end{pmatrix} + \begin{pmatrix} F^c \\ T^c \end{pmatrix} \quad (4)$$

$F$  and  $T$  are the force and torque vectors:  $F_H$  and  $T_H$  are the force and torque on a particle due to hydrodynamic interactions with other particles;  $F^c$  and  $T^c$  are the contact force and torque on a particle due to its contact with other particles, respectively. The hydrodynamic interactions along with the hydrodynamic stresslet  $S_H$  (required to calculate the excess hydrodynamic stress due to the presence of particles in a fluid) are obtained using the well-known resistance formulation

$$\begin{pmatrix} F_H \\ T_H \\ S_H \end{pmatrix} = -\eta_0 R \cdot \begin{pmatrix} U - U^\infty \\ \Omega - \Omega^\infty \\ -E^\infty \end{pmatrix} \quad (5)$$

where  $U$  and  $\Omega$  are the particle translational and rotational velocity vectors, respectively,  $\eta_0$  is the viscosity of the suspending fluid,  $R$  is the particle–particle configuration-dependent resistance matrix, and  $S_H$  is the hydrodynamic stresslet.  $U^\infty$ ,  $\Omega^\infty$ , and  $E^\infty$  are the translational, rotational, and elongational components of the imposed background flow on the suspension. At a

shear-rate,  $\dot{\gamma}$ , a simple shear flow corresponds to  $\Omega_{33}^\infty = -\frac{\dot{\gamma}}{2}$  and  $E_{12}^\infty = E_{21}^\infty = \frac{\dot{\gamma}}{2}$  while other elements are 0.

We split the resistance matrix  $R$  in two parts<sup>[41]</sup>

$$R = R_{\text{Stokes}} + R_{\text{lub}} \quad (6)$$

where  $R_{\text{lub}}$  is the two-body lubrication matrix obtained by pairwise adding all the lubrication interactions ( $h^{-1}$  and  $\log(h^{-1})$  terms, where  $h$  is the interparticle gap), and  $R_{\text{Stokes}}$  is a diagonal matrix containing terms which approximate the far-field many-body interactions.

We model the particle surface roughness as a hemispherical asperity with size  $h_r$  on the base particle surface as shown in the inset of **Figure 6**. The particles come into contact if the interparticle gap,  $h = d - (a_1 + a_2 + h_r)$ , becomes smaller than 0. Here,  $d$  is the particle center to center distance and  $a_1, a_2$  are the radii of the particles, and  $h_r$  is the roughness size. The contact between the particles via surface asperities results in normal,  $F_n^c$  and tangential forces,  $F_t^c$ , giving a net contact force  $F^c = F_n^c + F_t^c$  along with a torque  $T^c = \mathbf{a} \times F_t^c$ , where  $\mathbf{n}$  and  $\mathbf{t}$  give the normal and tangential directions. We calculate  $F_n^c$  using the Hertz contact law and  $F_t^c$  using a linear tangential spring as shown in **Figure 6**. Finally, contact interactions follow the Coulomb's law for friction  $|F_t^c| \leq \mu |F_n^c|$ , where  $\mu$  is the friction coefficient. To investigate the effects of varying the particle roughness on the suspension rheological behavior, we use a normal load dependent  $\mu = 0.27 \coth \left[ 0.27 \left( \frac{|F_n^c|}{k_n} \right)^{0.35} \right]$ , which has been measured experimentally and explains the shear-thinning behavior in dense suspensions.<sup>[43]</sup> **Figure 6** illustrates the particle contact model with contact forces and lubrication interactions.

Using these expressions for the hydrodynamic and contact interactions, we solve the force balance in Equation (4). We solve the following linear equations to calculate the particle velocities  $U$  and  $\Omega$

$$\eta_0 R \cdot \begin{pmatrix} U - U^\infty \\ \Omega - \Omega^\infty \\ -E^\infty \end{pmatrix} = \begin{pmatrix} F^c \\ T^c \end{pmatrix} \quad (7)$$

Once the particle velocities are known, we use forward time marching for updating the particle positions and repeat this procedure at each time step. We calculate the bulk stress tensor,  $\Sigma$ , by ensemble averaging the hydrodynamic and contact stresslet for each particle pair. The relative suspension viscosity  $\eta/\eta_0$  is

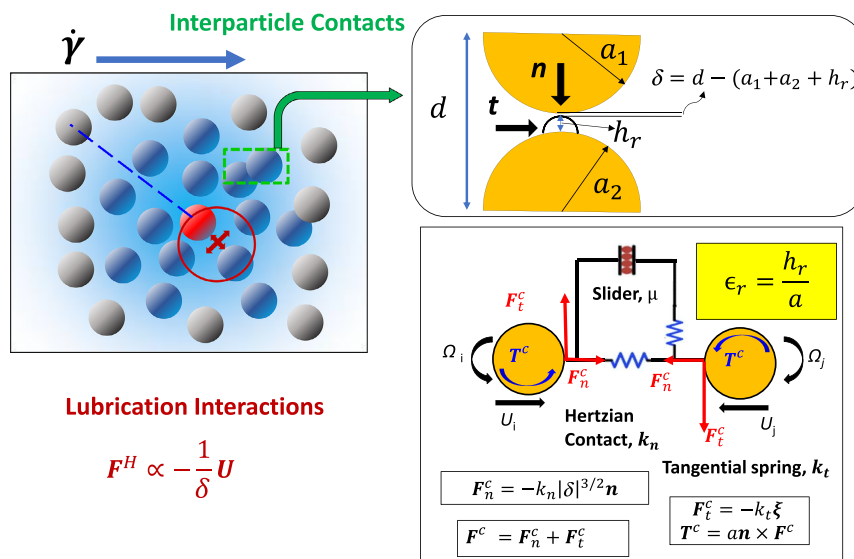


**Figure 6.** Schematic diagram showing particle lubrication interactions and contact model involving contact forces (normal and tangential:  $F_n^c$  and  $F_t^c$ , respectively), torque  $T^c$ , linear tangential spring stretch,  $\xi$ , and stiffness coefficients  $k_n$  (normal), and  $k_t$  (tangential), and  $h$  is the interparticle gap,  $h_r$  is the roughness size and  $a$  is the characteristic length scale for the simulations.

obtained as  $\frac{\eta}{\eta_0} = \frac{\Sigma_{12}}{\eta_0 \dot{\gamma}}$ . Here,  $\eta$  is the suspension viscosity. Further details on the numerical implementation and the procedure to calculate the stresslets can be found in the cited literature.<sup>[43–45]</sup>

Numerical simulations were performed for a surface roughness of up to 2% of the particle diameter. The simulations shown in **Figure 7** reproduce the shear-thinning behavior observed for the experimental systems. In agreement with experimental data of Figure 3, the simulation results of Figure 7 also show that increasing the particle roughness increases the pseudoplastic electrode material viscosity. This rise in the suspension viscosity with roughness is a consequence of increase in the average coefficient of friction between the contacting particles as roughness increases.<sup>[43]</sup> In addition, numerical simulations for suspensions in the low shear-rate regime show an increase in the storage modulus ( $G'$ ) with particle roughness ( $\epsilon_r$ ) for a high

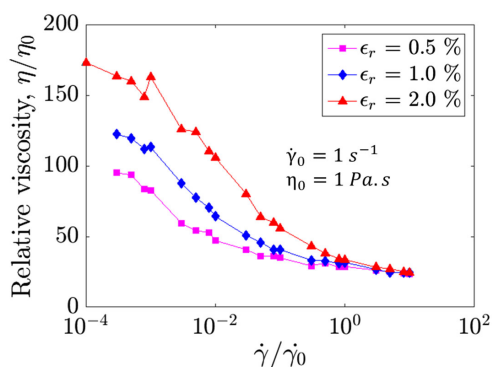


**Figure 7.** Numerical simulations showing relative viscosity versus shear-rate for different dimensionless particle roughness,  $\epsilon_r = h_r/a$ . Particle concentration is at 50% by volume. Here,  $\dot{\gamma}_0$ , which is a characteristic shear-rate scale has been used to scale the shear-rate,  $\dot{\gamma}$ , and we use a load dependent  $\mu = 0.27 \coth \left[ 0.27 \left( \frac{|F_n^c|}{k_n} \right)^{0.35} \right]$ .

concentration ( $\phi = 50\%$  by volume) Newtonian suspension (see **Figure 8**). This is a good representation of the solar cell's frontside grid metallization pseudoplastic paste behavior under high shear-rates, where it can be treated as a Newtonian fluid suspension with a high particle concentration.

### 2.3. Oscillatory Shear Tests

For frontside Ag grid pseudoplastic pastes, the storage modulus is greater than the loss modulus ( $G''$ ) at very low shear-rates, but as the shear-rate increases a crossover point is reached, where the loss modulus becomes greater than the storage modulus.<sup>[18]</sup> To understand the effect of the measured shear moduli on the thick-film gridline geometry, we consider the loss phase-angle, defined as,  $\delta = \tan^{-1}(G''/G')$ , as it is an important figure of merit, which indicates the amount of lost energy, or energy dissipated as heat, to the stored energy in the viscoelastic material. Basically,  $\delta$  is an

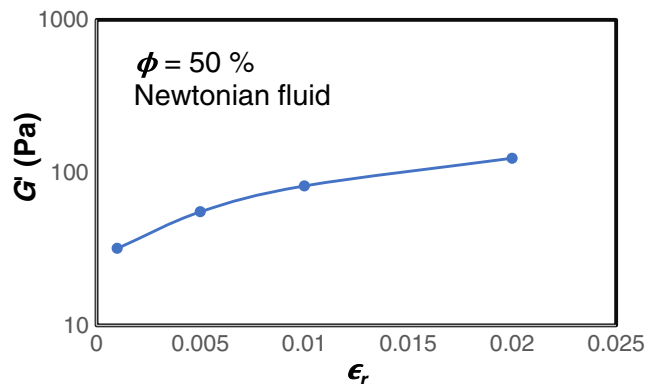


**Figure 8.** Numerically simulated storage modulus versus roughness for 50% particle concentration by volume with varying roughness size in the low shear-rate regime.

index of the contribution of the elastic and viscous components in the thick-film viscoelastic material, and it may be utilized to analytically assess AR of SP electrode metallization pastes. Hence, the loss phase-angle may be considered as an indication of the inefficiency of the viscoelastic paste's rheological shear flow behavior—higher  $\delta$  should result in lower AR, and vice versa. By studying the viscoelastic dynamic modulus behavior of the pastes under strain (shown in **Figure 9**) one can better understand which paste would yield an improved viscoelastic recovery and AR. Namely, the real and imaginary components of  $G^* = G' + iG''$  are measured. During shearing, beyond the  $G'-G''$  crossover point, in the range of strain from  $\approx 50\%$  to  $\approx 200\%$  for the group B pastes the loss modulus for the smooth Ag powder paste ( $G''_{B-s}$ ) is quite close to the loss modulus for the corrugated Ag powder paste ( $G''_{B-c}$ ) as shown in **Figure 9a**. On the other hand, as shown in the plots of **Figure 9a,b**, for both groups B and C, respectively, beyond the  $G'-G''$  crossover point the storage modulus for the smooth Ag powder pastes ( $G'_{B-s}$  and  $G'_{C-s}$ ) drops significantly more compared with the storage modulus for the corrugated Ag powder pastes ( $G'_{B-c}$  and  $G'_{C-c}$ ) particularly in the strain range of  $\approx 50\%$  to  $\approx 200\%$  and  $5\%$  to  $100\%$  for pastes B and C, respectively. However,  $G''_{C-s}$  is relatively not as significantly lower compared with  $G''_{C-c}$  for group C pastes (see **Figure 9b**). Hence, for both paste groups B and C, we have  $\tan(\delta_s) > \tan(\delta_c)$ , hence,  $\delta_s > \delta_c$ , where  $\delta_s$  and  $\delta_c$  are the loss phase-angles for the smooth- and corrugated-surface Ag powder pastes, respectively. The smooth Ag powder paste has more dampening, which is basically an increased ratio of heat dissipation energy to the maximum stored energy in the viscoelastic Ag paste material, compared with the corrugated Ag powder paste. Therefore, the viscoelastic recovery behavior as well as the associated AR are expected to be more significant for the corrugated Ag powder paste compared with the smooth Ag powder paste. This viscoelastic behavior due to the corrugated Ag powder topography generally results in an increase in shear stress.

We can also conclude that the viscoelastic effects of powder surface topography hold regardless of the viscosity and degree of thixotropy of the metal powder pseudoplastic pastes, but for higher viscosity more thixotropic pastes the differences in print quality and electrical performance should be readily observed at

lower shear-rates or print-speeds, and lower strain (%). However, for less thixotropic and less viscous pastes the differences in the viscoelastic behavior are generally better observed at higher shear-rates, higher print-speeds, and thus, higher strain (%) as shown by the rheology measurements in **Figure 9a,b**. The solar cell metallization Ag pastes behave as a Newtonian fluid at high shear-rates, and our experimental results showing improvement of  $G'$  at high shear-rates for corrugated Ag powder pastes (as shown in **Figure 9**) agree with the numerical simulation result of **Figure 8**.

The improved shear storage modulus may be explained by enhanced trapping of solvent and polymer solution (organic vehicle) within or in-between the Ag powders during shearing. This behavior can be explained based on the following formula, which quantifies the shear storage modulus,  $G'_p$ , of the rubbery polymeric material at a temperature,  $T$ <sup>[47]</sup>

$$G'_p = \left( \frac{\rho RT}{M_e} \right) V_p^2 \quad (8)$$

where  $\rho$  is the density of the polymer solution,  $M_e$  is the molecular weight of the organic material between Ag particles and Ag powder asperities,  $V_p$  is the trapped volume fraction of the polymer solution in-between the Ag powders and Ag powder asperities, and  $R$  is the molar gas constant. The molar or ideal gas constant appears in the formula based on the assumption that an ideal rubbery material behaves in a way like that of an ideal gas network. During screen printing, the sheared paste temperature is expected to increase due to friction between the solid particles. The measured storage modulus,  $G'$ , was found to increase for corrugated Ag powder pastes compared with smooth Ag powder pastes for the measured temperature range of interest, as shown in **Figure 10**. This result supports the hypothesis that corrugated-surface Ag powders aid in enhancing the volume fraction of the trapped polymer solution. Measurements were taken at 100% strain for group B pastes and 25% strain for group C pastes, which are representative of strain levels experienced by the Ag pastes under shearing. In general, the increase of  $G'$  with increasing temperature for the corrugated-surface Ag powder paste may be an indication that Ag powder asperities can better trap solvents and polymer solution compared with

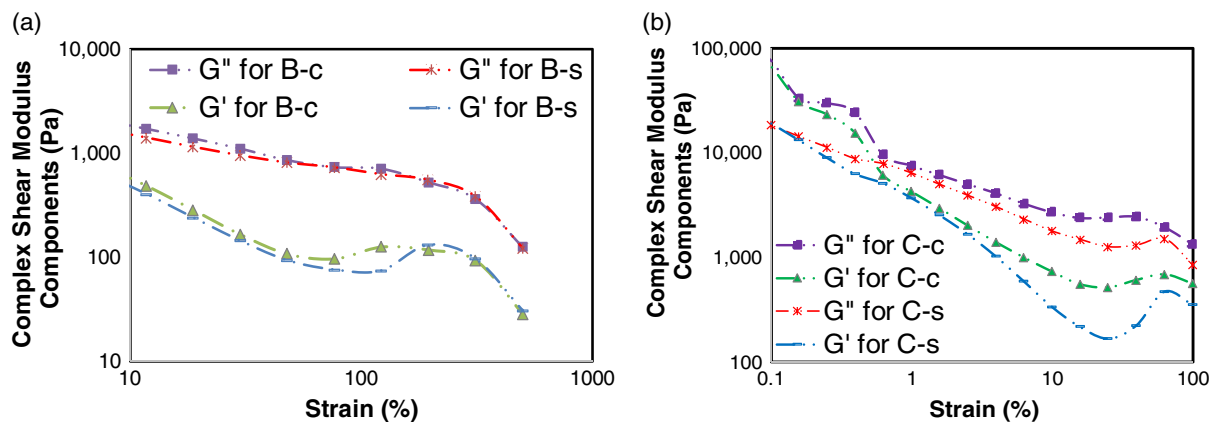


**Figure 9.** Shear modulus versus strain (%) for pseudoplastic electrode materials with smooth- and corrugated-surface Ag particles, for a) group B, and for b) group C pastes. Plots are shown after the  $G'-G''$  crossover point. Part (b): Adapted with permission.<sup>[40]</sup> Copyright 2018, IEEE.

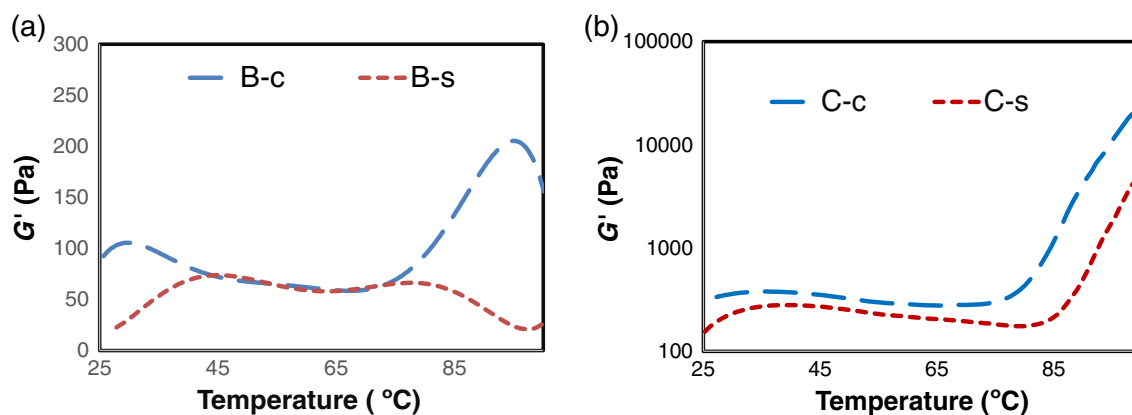


**Figure 10.** Shear storage modulus versus temperature for the corrugated- and smooth-surface Ag powders for a) group B electrode paste material under 100% strain, and b) group C electrode paste material under 25% strain. Part (b): Adapted with permission.<sup>[40]</sup> Copyright 2018, IEEE.

smooth-surface Ag powders, which do not have this ability. As the temperature rises above room temperature,  $G'$  almost linearly increases for all pastes. Beyond 40 °C volatile thinner/solvent decreased density with temperature may cause the slight gradual drop in  $G'$  for both types of pastes with different Ag powder topographies. Then, the increase in temperature is compensated by a drop in the density of the solvents in the paste resulting in an almost stagnant or gradually decreasing  $G'$ . Starting at  $\approx 70$  °C the polymer solution viscosity drops significantly behaving like a Newtonian fluid; consequently, it should be more easily trapped in-between asperities, increasing  $G'$  at higher temperature as shown in Figure 10a for corrugated Ag powder paste. Also, as shown in Figure 10b, this behavior of increasing  $G'$  in the temperature range of  $\approx 70$ –95 °C is observed for both smooth and corrugated Ag powder pastes, only for the more thixotropic, higher viscosity polymer solution of group C pastes. In this case, with higher temperature the polymer solution may provide more viscoelasticity under shearing within the polydisperse Ag powder phase, even for the smooth Ag powders, thus causing an increase in  $G'$  for both group C pastes compared with group B pastes, where  $G'$  increases for the corrugated Ag powder paste only in this temperature range.

## 2.4. Gridline-Definition Analysis

In this section, gridline geometry is studied using 3D microscope analysis. **Figure 11** shows the 3D top-view of the solar cell SP gridlines. The results generally show that screen printing Ag pastes at higher print-speeds can yield regions with less amount of deposited electrode material than the case for slower print-speeds as shown when comparing Figure 11a,b, and Figure 11c,d, for thick films SP at 250 mm s<sup>-1</sup> versus those SP at 500 mm s<sup>-1</sup>. We also notice that at high print-speeds of 500 mm s<sup>-1</sup> thick-film electrode materials with smooth Ag powders are more prone to discontinuities in the printed gridline (see Figure 11b) compared with the corrugated Ag powder paste gridline shown in Figure 11d. For better understanding of the SP gridline topography, we study the side-view images of thick-film gridlines for smooth and corrugated Ag powders for group B and group C Ag pastes. As shown in Figure 11e–h, for both group B

and group C Ag pastes, corrugated Ag powders result in less variation in the gridline height with less peak-to-valley difference.

By measuring the gridline dimensions at six different positions on the solar cell metallization grid, we obtained the average, maximum, and minimum grid line height and width for group B and group C Ag paste thick films, SP at 500 and 150 mm s<sup>-1</sup>, respectively. As shown in **Table 2**, the difference between gridline height maxima (peaks) and minima (troughs) is larger for smooth Ag powder electrodes for both paste groups in agreement with the images of Figure 11e–h. Regardless of the electrode Ag paste material viscosity, we observe that corrugated Ag powder has a positive effect on improving the AR of the printed gridline. This analysis confirms that the increase in shear storage modulus helps result in an improvement in viscoelastic recovery of the SP thick film. For group C electrode material SP at a speed of 150 mm s<sup>-1</sup>, the AR is on average improved from  $\approx 0.29$  to  $\approx 0.38$  when going from smooth to corrugated Ag powder thick-film gridlines, respectively. On the other hand, for group B electrode material SP at a faster speed of 500 mm s<sup>-1</sup>, the AR is on average improved from  $\approx 0.36$  to 0.42 when going from smooth to corrugated Ag powder thick-film gridlines, respectively. Group B and group C Ag pastes were SP through 28 and 34  $\mu\text{m}$  screen finger openings, respectively, as group B Ag pastes are easier to print at high print-speeds through narrower screen openings compared with group C Ag pastes. Hence, in agreement with the oscillatory rheometry data, the line-definition data of Table 2 and the microscope images of Figure 11 show that the dimensions for printed gridlines containing corrugated-surface Ag powders yield an improved average height and AR (Table 2b,d), while the gridline-definition data shown in Table 2a,c indicates lower average AR for the SP gridlines containing smooth Ag powders. In addition, smooth-surface Ag powders show larger differences between minima and maxima in gridline height, as illustrated by the 3D microscope images and measurements in Figure 11 and Table 2, respectively. Less variations in height along the gridline are desirable for achieving good print quality with less chance of gridline discontinuity defects, particularly for long-time screen printing in large-volume production.



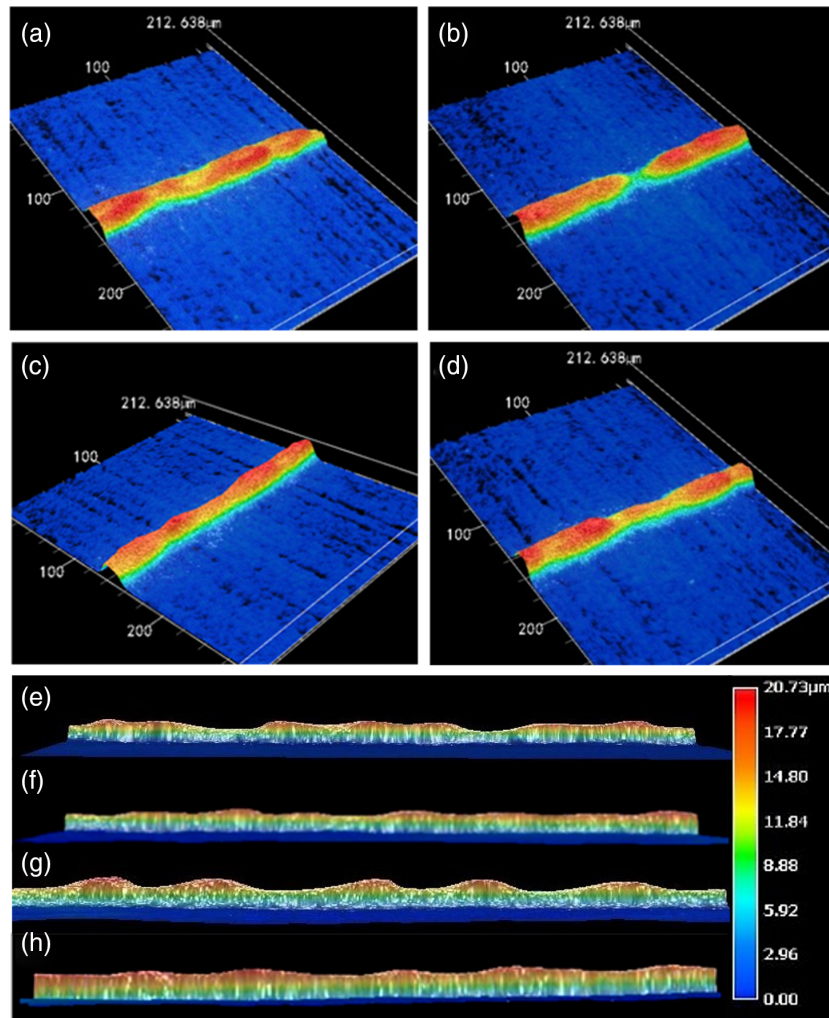


**Figure 11.** Top-view 3D microscope images for paste B-s thick-film gridlines SP at a) 250 mm s<sup>-1</sup>, b) 500 mm s<sup>-1</sup>, and for paste B-c thick-film gridlines SP at c) 250 mm s<sup>-1</sup>, and d) 500 mm s<sup>-1</sup>. Gridline 3D microscope side-view images for Ag pastes SP at 500 mm s<sup>-1</sup> for e) paste B-s gridlines, and f) paste B-c gridlines; as well as Ag pastes SP at 150 mm s<sup>-1</sup> for g) paste C-s gridlines, and h) paste C-c gridlines. Parts (g,h): Adapted with permission.<sup>[40]</sup> Copyright 2018, IEEE.

**Table 2.** Gridline height and width, average, maximum, and minimum values for group B pastes with a) smooth, and b) corrugated Ag powders SP at 500 mm s<sup>-1</sup> print-speed; and group C pastes with c) smooth, and d) corrugated Ag powders SP at 150 mm s<sup>-1</sup> print-speed. Parts (c,d): Adapted with permission.<sup>[40]</sup> Copyright 2018, IEEE.

| a)      | Line height<br>[μm] | Line width<br>[μm] | c) | Line height<br>[μm] | Line width<br>[μm] |
|---------|---------------------|--------------------|----|---------------------|--------------------|
| Average | 11.7                | 32.0               |    | 14.3                | 49.5               |
| Minimum | 3.3                 | 25.7               |    | 10.1                | 39.3               |
| Maximum | 17.2                | 38.5               |    | 19.5                | 58.0               |
| b)      |                     |                    | d) |                     |                    |
| Average | 12.9                | 30.4               |    | 17.4                | 45.7               |
| Minimum | 9.3                 | 21.4               |    | 14.2                | 38.2               |
| Maximum | 18.4                | 38.9               |    | 21.1                | 51.4               |

## 2.5. Solar Cell Current–Voltage Measurements

As shown in **Figure 12** and **13**, on average the short-circuit current density ( $J_{sc}$ ) improved by 0.064 mA cm<sup>-2</sup> (Figure 12a) and 0.15 mA cm<sup>-2</sup> (Figure 13a) for the solar cells fabricated with group B and group C corrugated Ag powder pastes, respectively, compared with solar cells fabricated with their smooth Ag powder paste counterparts. The open-circuit voltage ( $V_{oc}$ ) was also improved for solar cells with corrugated-surface Ag powder electrodes for both groups B and C Ag pastes as shown in Figure 12b and 13b, respectively. The  $V_{oc}$  improvement for the solar cells fabricated with corrugated Ag powder electrode material is expected to be the result of lower recombination at the grid metal/Si interface yielding lower metal saturation current density ( $J_{oem}$ ) and possibly slightly lower junction leakage as well; however, this analysis is beyond the scope of this article. The average measured line-resistivity of sintered smooth-surface Ag powders

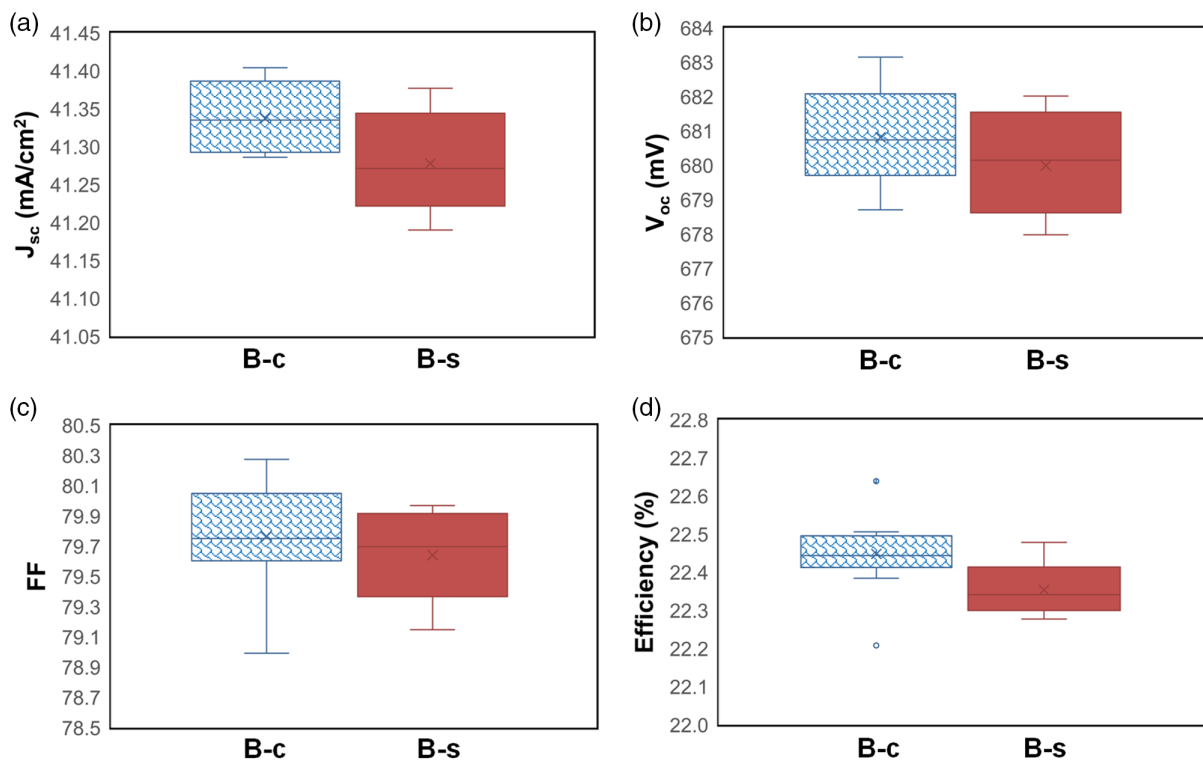


**Figure 12.** Electrical  $I$ – $V$  data for PERC monocrystalline-Si solar cells with SP gridlines using group B pastes with corrugated-surface and smooth-surface Ag powders: a) short-circuit current density ( $J_{sc}$ ), b) open-circuit voltage ( $V_{oc}$ ), c) FF, and d) conversion efficiency (%).

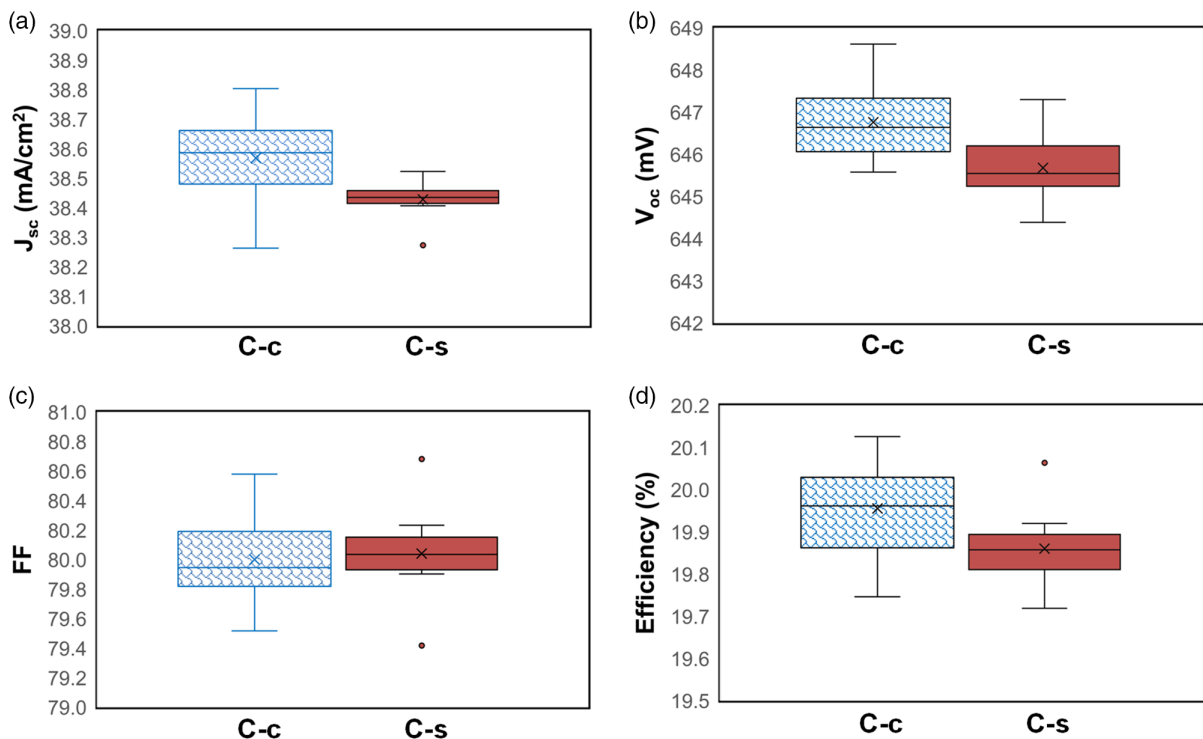


**Figure 13.** Electrical  $I$ – $V$  data for Al-BSF monocrystalline-Si solar cells with SP gridlines using group C pastes with corrugated-surface and smooth-surface Ag powders: a) short-circuit current density ( $J_{sc}$ ), b) open-circuit voltage ( $V_{oc}$ ), c) FF, and d) conversion efficiency (%). Adapted with permission.<sup>[40]</sup> Copyright 2018, IEEE.

and corrugated-surface Ag powders is  $\approx 2.2$  and  $2.6 \mu\Omega \text{ cm}$ , respectively, this indicates slightly enhanced Ag gridline bulk densification during the sintering process of the smooth-surface Ag powders, most likely due to the higher percentage of finer Ag powders (see Figure 2).<sup>[33]</sup> Nevertheless, when considering the overall solar cell series resistance ( $R_s$ ), the corrugated Ag powder electrode material performs at least as good as the smooth-surface Ag powder electrode material (see Figure 14). This may be an indication of a somewhat lower contact resistivity at the frontside grid Ag–Si interface for the corrugated-surface Ag powders because Si solar cell bulk, emitter sheet resistance, and backside electrode are identical for comparative experiments involving both Ag powder surface topographies. More in-depth analytical characterization is needed to understand and validate these conclusions regarding the electrical contact resistivity of the gridlines. As shown in Figure 12c, fill factors (FFs) of group B thick-film electrode materials with the two different Ag powder topographies are slightly better for solar cells with the corrugated Ag powder electrode material compared with those with smooth-surface Ag powder electrode material. For group C electrode materials, the solar cell FFs are similar for both Ag powder topographies as shown in Figure 13c. This may indicate that the junction quality for the solar cells with the corrugated Ag powder grid metallization is at least as good as that of solar cells with smooth Ag powder grid metallization, particularly because  $R_s$  is remarkably similar for both Ag powder topographies for both groups B and C electrode materials, as shown in Figure 14a,b. For groups B and C electrode materials, the conversion efficiency improvement for solar cells with corrugated Ag powder electrode thick films was on average  $\approx 0.1\%$  absolute higher than solar cells made with smooth-surface Ag powder grid metallization (see Figure 12d and 13d, mainly due to the improvement in  $J_{sc}$ ). Although  $0.1\%$  efficiency improvement may not seem to be very significant; nevertheless, for large-scale PV power plants this difference translates into a substantial amount of power gain without added costs.

## 2.6. Optical Simulation

To understand the reason for the improved photocurrent in solar cells with thick-film frontside grid formed from corrugated Ag powders, optical ray-tracing simulations are performed. For the simulations, we obtained high-definition cross-sectional

profile images of the low and high sections of the gridlines for both electrode materials made from corrugated and smooth Ag powders (see Figure 15). As shown in Figure 15, the low and high regions of the gridline have smaller (Figure 15a,c) and larger cross-sectional areas (Figure 15b,d), respectively, and they are representative of the periodic nature of the gridline geometry across the solar cell. Group B Ag paste was chosen for optical simulations because it was used for fabricating the PERC Si solar cell frontside grid metallization at high print-speeds that are currently used in the PV industry. The right and left regions of the gridline cross-sectional profile appear to be more symmetric particularly at the peak of the larger-area cross section of the corrugated Ag thick-film gridline (Figure 15d) compared with the larger-area cross section of the smooth Ag thick-film gridline (Figure 15b).

Ray-tracing simulations were performed to calculate contact redirection dependent on the geometry of the contact gridline (see Figure 16) for ideal specular and ideal diffuse reflection, respectively. The fabricated contacts have a spectrum dependent reflectance, which is partially diffuse and partially specular. The wavelength-dependent diffuse and specular reflection is shown in Figure 16a. It is apparent that diffuse reflection dominates. We performed ray-tracing simulations for both specular and diffuse conditions for which we developed an algorithm that performs reflector-centric reverse ray-tracing simulations.<sup>[48]</sup> Two example ray distributions for specular reflection are shown in Figures 16b,c. The solar cell surface is shown as a red line on the top and rays are incident from the bottom. The blue curves show the contour of the contacts. Figure 16b shows the left side of sample B-s2 (smaller cross-sectional profile for smooth-surface Ag powder gridlines). Due to the low AR, all rays are reflected into the lower hemisphere, i.e., the contact does not redirect through specular reflection. However, in Figure 16c, the same situation is shown for the right side of sample B-s3 (larger cross-sectional profile for smooth-surface Ag powder gridlines). It is shown that some of the rays are reflected toward the solar cell surface, and therefore the contact partially redirects light in a specular way. For the diffuse reflection properties, the algorithm fully accounts for view-factor shading, but not for second order reflections. In other words, only rays with an unobstructed view from a point on the contact to the solar cell are being simulated as visualized in Figure 16d–f. The geometric redirection as determined by these simulations is slightly higher

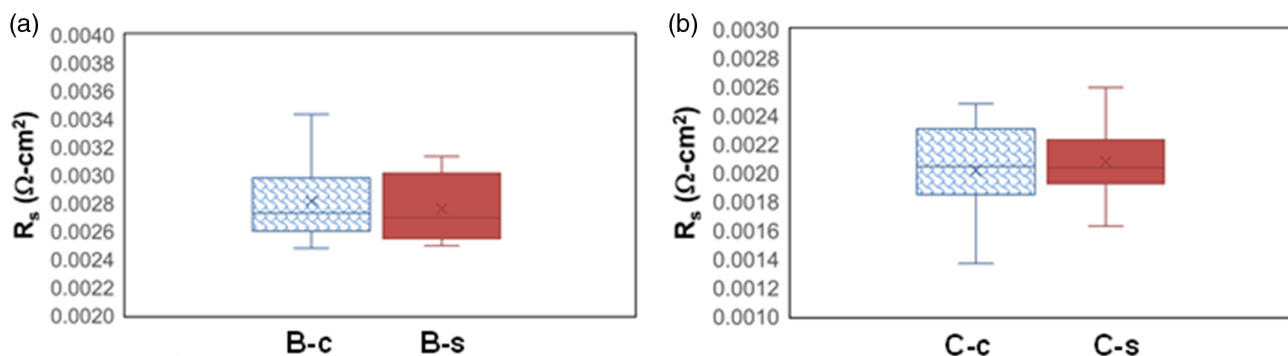


**Figure 14.** Series resistance boxplots for a) PERC monocrystalline-Si solar cells with SP gridlines using group B Ag pastes, and b) Al-BSF monocrystalline-Si solar cells with SP gridlines using group C Ag pastes for corrugated- and smooth-surface Ag powders.

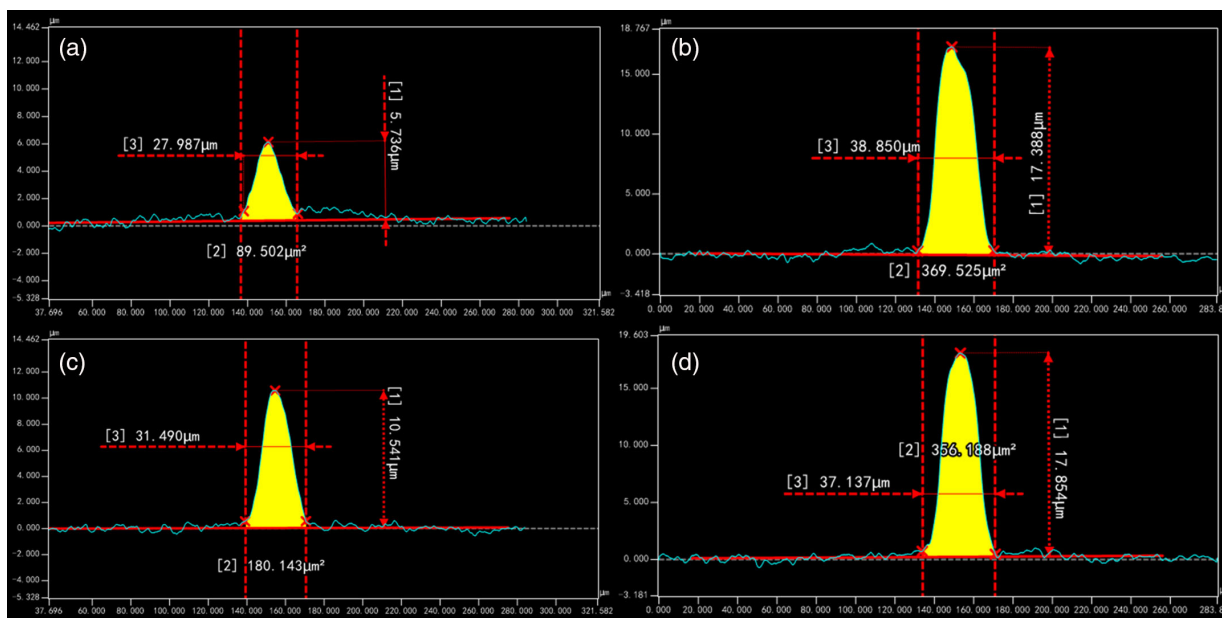


**Figure 15.** Gridline cross-sectional profiles for group B electrode paste with smooth Ag powder at a) smaller and b) larger cross-sectional regions of the gridline geometry, and corrugated Ag powder electrode material at c) smaller and d) larger cross-sectional regions of the gridline geometry. The Ag pastes were SP at a print-speed of  $500 \text{ mm s}^{-1}$  through  $28 \text{ }\mu\text{m}$  grid pattern finger openings of the screen.

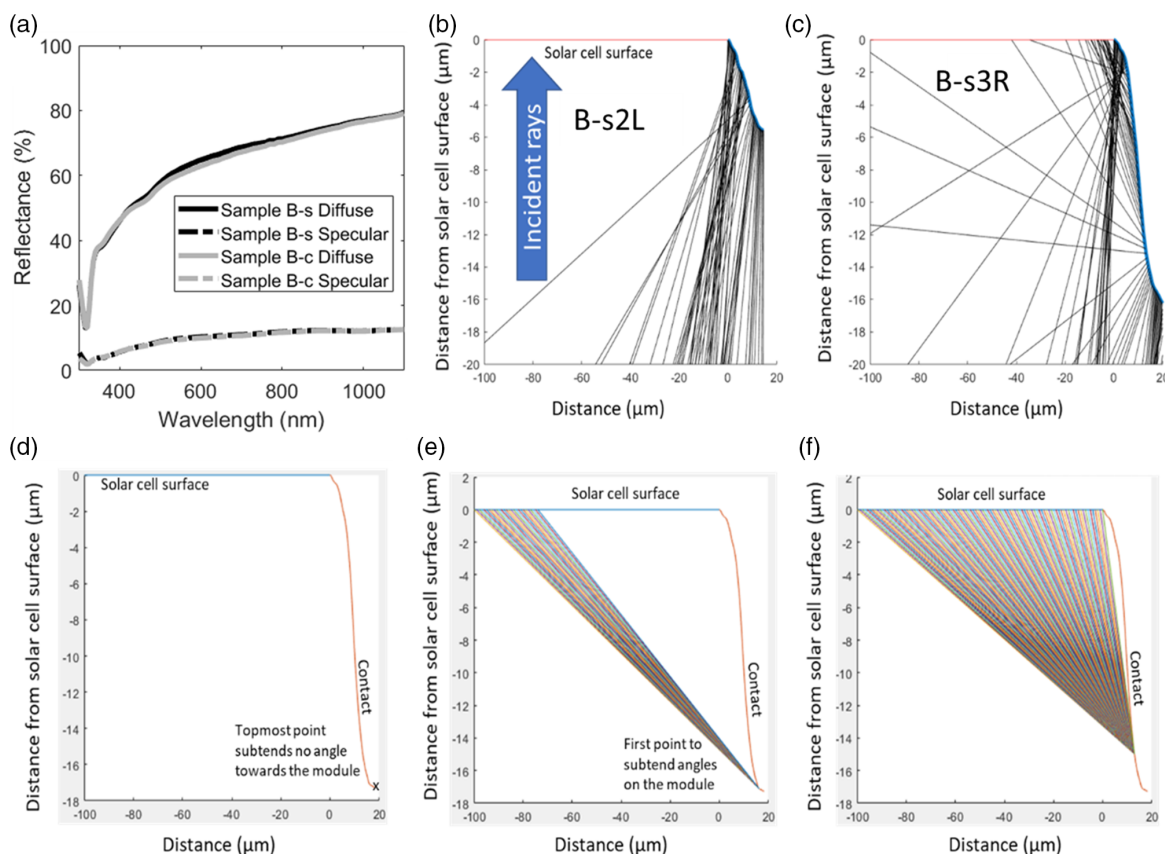


**Figure 16.** a) Measured diffuse and specular reflectance of the silver used for sample B-s and B-c. Visualization of the rays reflected in a specular way from b) the left side of contact B-s2 (B-s2L) and c) the right side of B-s3 (B-s3R). The red line shows the solar cell surface and the blue line the contour of the contact. d–f) The rays originating from diffuse reflection on different positions of the contact. The simulation only accounts for rays with unobstructed view to the solar cell.

**Table 3.** a) Geometric redirection factor in % for gridline geometry. B-s2 and B-s3 indicate smaller and larger cross-sectional profiles for smooth-surface Ag powder electrodes, and B-c2 and B-c3 indicate smaller and larger cross-sectional profiles for corrugated-surface Ag powder electrodes, respectively. b) Geometric redirection factor in % for gridline geometry from (a). R and L indicate the right and left sides of the gridline profiles, respectively.

| a)       | B-s2  |       | B-s3  |       | B-c2  |       | B-c3  |       |
|----------|-------|-------|-------|-------|-------|-------|-------|-------|
| Diffuse  | 10.52 |       | 13.10 |       | 11.59 |       | 14.17 |       |
| Specular | 0.00  |       | 18.25 |       | 9.71  |       | 18.39 |       |
| b)       | B-s2L | B-s2R | B-s3L | B-s3R | B-c2L | B-c2R | B-c3L | B-c3R |
| Diffuse  | 6.76  | 3.76  | 6.57  | 6.53  | 5.66  | 5.93  | 7.66  | 6.51  |
| Specular | 0.00  | 0.00  | 7.06  | 11.19 | 9.34  | 0.37  | 9.29  | 9.10  |

for gridlines made from corrugated-surface Ag powder electrode material (sample B-c) compared with the smooth-surface Ag powder electrode material (sample B-s) as shown in Table 3. In particular, the smaller cross-sectional profile regions of sample B-s show no specular redirection as all rays are reflected away from the solar cell (see Figure 16b); on the other hand, the smaller cross-sectional gridline regions of sample B-c do show noticeable specular redirection. To obtain the full redirection under AM1.5, the geometrical redirection can be multiplied with spectrum-dependent reflectance and weighted with the AM1.5 spectrum.

### 3. Conclusion

The SP solar cell frontside grid metallization paste formulation is a complex material system that can have several rheological features based on the different properties of the various ingredients in the Ag paste. Henceforth, precise optimization of the SP frontside electrode Ag paste composition to achieve highest solar cell performance levels is a nontrivial objective. In this research work, through a comparative study of the Ag powder surface topography it was possible to demonstrate an effective improvement in the quality and viscoelastic characteristics of the SP Ag paste resulting in a consistently reproducible enhancement of solar cell gridline AR, cross-sectional symmetry, and resolution. Depending on the organic vehicle used in the Ag paste, gridline AR improvement in the range of  $\approx 10\%$  to  $\approx 30\%$  was attained for SP thick-film electrode metallization having Ag powders with surface asperities. Moreover, due to enhanced storage modulus and viscoelastic recovery, solar cell frontside metallization gridlines composed of sintered rough-surface Ag powders showed less dimensional variations in height in comparison with the SP thick-film electrode metallization with Ag powders having smooth surfaces. This enhanced gridline geometry led to a  $0.14 \text{ mA cm}^{-2}$  average increase in  $J_{sc}$ , which largely contributed to  $\approx 0.1\%$  absolute efficiency improvement for large-area monocrystalline Si solar cells with Al-BSF allowing for greater than 20% solar cell conversion efficiencies to be achieved. Similarly, for large-area monocrystalline Si PERC solar cells, the improved gridline geometry led to a  $0.064 \text{ mA cm}^{-2}$  average increase in  $J_{sc}$ , which also contributed to a conversion efficiency

improvement of  $\approx 0.1\%$  absolute resulting in 22.45% average solar cell conversion efficiency. This was mainly achieved through the improvement of the dynamic oscillatory shear rheological behavior at higher shear-rates for the Ag electrode pseudoplastic paste rather than by increasing static yield stress. This study demonstrates a way forward for improving the AR of fine-line SP Ag paste metallization while simultaneously improving the printability (or print quality) for high-speed printing used in the PV industry. From this work, it can be concluded that we need to design electrode shear-thinning materials with enhanced Ag powder roughness using finer Ag powders to allow for easier printing through narrower screen finger openings and to exhibit good thixotropic behavior at the same time—ultimately, allowing for good line definition and high AR. This study can also help enhance the fundamental scientific understanding of SP paste rheological behavior and associated effects on optical redirection for ultrafine-line high AR gridline metallization, which can enable higher industrial c-Si solar cell conversion efficiencies to be achieved in the future.

### 4. Experimental Section

Different silver powders with smooth and rough, or corrugated, surface topography were studied for comparison. For the corrugated Ag powder surface topography, the powders have corrugations in the nanoscale; the peak-to-valley height of the surface asperities (surface roughness) is typically around 4.5% of the particle diameter. On the other hand, the smooth-surface Ag particle is relatively dense, and the surface roughness is typically  $\leq 0.5\%$  of the particle diameter. For the experimental comparative studies conducted in this work, in order to minimize the impact of yield stress and zero-shear viscosity factors on the SP line definition as much as possible, particle-size distributions were selected to have overall specific-surface-area (SSA) in a close range: at least  $\approx 0.35$  to at most  $\approx 0.4 \text{ m}^2 \text{ g}^{-1}$  for the smooth- and rough-surface Ag powders, respectively, with identical vol% content in the electrode paste materials. The spherical silver powders were synthesized using a “phase build-up” process involving chemical precipitation and aggregation techniques of metal particles.<sup>[49–51]</sup> Particle-size distribution analysis was performed using a Malvern Mastersizer 3000 laser-diffraction particle-size analyzer. Rheological analysis was performed using an R/CPS + Brookfield rotational rheometer, as well as an Anton Paar MCR 301 oscillatory rheometer. Various electrode pseudoplastic Ag pastes with different viscosities and thixotropic levels were evaluated to study the effect of corrugated Ag powder surface versus a smooth Ag powder surface on the rheological behavior. As a reference for the various Ag pastes studied viscosity measurements were performed at 10 rpm at a temperature of 25 °C using a Brookfield DVIII viscometer with a V74 vane spindle. Yield stress of SP pastes was evaluated by plotting the shear stress versus shear-rate as reported by Cheng and Lapasin et al.,<sup>[52,53]</sup> using the Brookfield rotational rheometer with controlled deformation step changes to obtain the nonzero shear-rate after timed-shear and waiting-time steps. In this work, thixotropy is evaluated by measuring the enclosed area between the up- and down-curve that is obtained in a linearly increasing or decreasing shear-rate over time—this is basically the hysteresis loop in the shear stress versus shear-rate plot.<sup>[54]</sup>

The wt% composition of the Ag pastes investigated in this work is as follows:  $\approx 89\%$  Ag powder, 2–3% glass frit,  $\approx 7\%$  organic vehicle,  $\leq 1\%$  surfactant, and  $\leq 1\%$  thinner solvent. To fabricate the Ag pastes, the organic vehicle is first formulated whereby a polymer solution is synthesized by mixing ethyl cellulose resin, a glycol ether solvent, and a plasticizer at about  $\approx 70 \text{ }^\circ\text{C}$  for  $\approx 20$  min. To complete the organic vehicle fabrication, a thixotropic agent is then added to the polymer solution and both constituents are blended using a high-shear mixer, which also activates the thixotropic agent. The paste constituents (thinner solvent,

surfactant, organic vehicle, glass frit, and Ag powder) are then mixed and homogenized in a vacuum planetary mixer. Subsequently, the mixture is passed through a 3-roll mill. The Ag pastes are then filtered and homogenized in a vacuum planetary mixer. The pastes were also manually stirred for 5 min immediately preceding the application of the pastes on the screen to ensure homogenization for screen printing. Three groups of pseudoplastic electrode materials (Ag pastes) with rough/corrugated and smooth Ag powder topography were studied and they are classified in terms of their rheology: group A—smooth Ag powder paste with lower viscosity,  $\approx 187$  Pa s, and lower thixotropy; group B—smooth Ag powder paste with intermediate viscosity,  $\approx 238$  Pa s, and intermediate thixotropy; and group C—smooth Ag powder paste with higher viscosity,  $\approx 266$  Pa s, and higher thixotropy. The Ag pastes are designated as follows: paste A-s with smooth-surface Ag powders and A-c with corrugated-surface Ag powders—both of which comprise group A rheology pastes; paste B-s with smooth-surface Ag powders and B-c with corrugated-surface Ag powders—both of which comprise group B rheology pastes; and paste C-s with smooth-surface Ag powders and C-c with corrugated-surface Ag powders—both of which comprise group C rheology pastes.

For stress and viscosity rheological measurements as a function of shear-rate, the measuring temperature is 25 °C. The measuring time for each measured point is 1 s, and the flow curve shear-rate is within a range of 6 to 360 1/s with 120 measured points. For the yield stress measurement, a preshear is performed at 100 1/s for 30 s followed by a waiting time of 120 s, which is followed by the shear stress measurements for yield stress extraction with a measuring time of 1 s for each measured point. For complex shear modulus real and imaginary components measurements as a function of strain %, the measuring temperature is 30 °C. Moduli data were collected in a logarithmic manner, 5 points per decade between 0.001% and 500% strain for pastes B-c and B-s with a total of 29 measured points at an angular frequency of 10 rad s<sup>-1</sup>. For pastes C-c and C-s, moduli data were collected in a logarithmic manner, 5 points per decade between 0.001% and 100% strain with a total of 26 measured points at an angular frequency of 6.28 rad s<sup>-1</sup>. An angular frequency of 10 rad s<sup>-1</sup> was used for all the temperature-sweep measurements with a measurement time of  $\approx 17.6$  s for each measured point with 141 measured points for pastes B-c and B-s while 99 points were measured for pastes C-c and C-s. To deposit the solar cell grid metallization, the different pseudoplastic electrode paste materials were SP at a squeegee speed of 150 and 500 mm s<sup>-1</sup> for groups C and B Ag pastes, respectively. Group B pastes can be more easily printed through narrower screen finger openings compared with group C pastes. Narrower gridline screen printing requires higher mesh screens with finer wire diameters, while wider gridlines can be SP using lower mesh screens, which require thicker wire diameters. Hence, group B pastes were SP using a standard 480-mesh screen with 11  $\mu$ m wire diameter and  $\approx 11$   $\mu$ m screen emulsion-coating thickness and 28  $\mu$ m finger openings while group C Ag pastes were SP using a standard 360-mesh screen with 16  $\mu$ m wire diameter and  $\approx 11$   $\mu$ m emulsion-coating thickness and 34  $\mu$ m finger openings. The Ag pastes were subsequently dried and fired in an in-line belt-furnace with infrared radiation-lamp heating. Group C Ag pastes were SP to form the frontside metallization grid for conventional Al back-surface field (BSF) Czochralski (Cz) monocrystalline Si large-area ( $\approx 244$  cm<sup>2</sup>) commercial solar cells, while group B Ag pastes were SP to form the frontside metallization of PERC Cz monocrystalline Si large-area ( $\approx 252$  cm<sup>2</sup>) solar cells. Except for the Ag spherical powders with the different surface topographies, paste formulations were identical for each group of pastes investigated. In other words, the contents and compositions of the glass frit, Ag powder, organic vehicle, additives, and surfactants were identical for every paste within each paste group studied. The Ag paste drying condition was 200 °C for 2 min. And for contact metallization, a spike-firing profile was used with an actual peak firing temperature of 780 °C for 1.5 s at a belt speed of 11 m min<sup>-1</sup>. Solar cell gridline print quality was characterized using a Keyence VHX-5000 3D microscope, while detailed cross-sectional profiles for the fired gridlines of the SP electrode materials were characterized using a Keyence VKX-1100 laser 3D microscope. For confirming the validity of our optical simulations, silicon nitride reflectance and redirection gridline reflectance as well as external quantum efficiency measurements were

performed using a Bentham IVT PVE300 quantum efficiency (QE) and reflectance (specular and diffuse) measurement tool. The electrical parameters and conversion efficiencies of the PV cells were obtained using a pulsed solar simulator, PSS 10 II, manufactured by Berger Lichttechnik GmbH & Co., which has automatic in-line solar cell current–voltage (*I*–*V*) testing and sorting capabilities. Solar cell series resistance values are obtained from the slope of the *I*–*V* curve at the open-circuit voltage point. Ten large-area (>100 cm<sup>2</sup>) solar cells were fabricated and tested for each case.

## Acknowledgements

Open access funding was enabled by Ganjiang Innovation Academy, CAS.

## Conflict of Interest

The authors declare no conflict of interest.

## Data Availability Statement

The data that support the findings of this study are available from the corresponding author upon reasonable request.

## Keywords

conductive materials, photovoltaic cells, rheology, surface topography, thick films

Received: August 19, 2021

Revised: October 2, 2021

Published online:

- [1] International Technology Roadmap for Photovoltaic (ITRPV), 11th ed., **2020**, <https://itrvp.vdma.org/>
- [2] R. Saive, H. A. Atwater, *Opt. Express* **2018**, 26, A275.
- [3] M. Green, *Joule* **2019**, 3, 631.
- [4] G. Kavlak, J. McNerney, J. E. Trancik, *Energy Policy* **2018**, 123, 700.
- [5] D. Erath, S. Pingel, R. Khotimah, A. De Rose, D. Eberlein, T. Wenzel, S. Order, A. Lorenz, F. Clement, *AIP Conf. Proc.* **2021**, 2367, 020006.
- [6] R. E. Trease, R. L. Dietz, *Solid State Technol.* **1972**, 15, 39.
- [7] S. B. Rane, P. K. Khanna, T. Seth, G. J. Phatak, D. P. Amalnerkar, B. K. Das, *Mater. Chem. Phys.* **2003**, 82, 237.
- [8] C. Ballif, D. M. Huljić, G. Willeke, A. Hessler-Wyser, *Appl. Phys. Lett.* **2003**, 82, 1878.
- [9] C. P. Hsu, R. H. Guo, C. C. Hua, C.-L. Shih, W.-T. Chen, T.-I. Chang, *J. Polym. Res.* **2013**, 20, 277.
- [10] J. Qin, W. Zhang, Z. Liu, S. Bai, *Int. J. Mod. Phys. B* **2015**, 29, 1540027.
- [11] J. Qin, S. Bai, W. Zhang, Z. Liu, H. Wang, *Circuit World* **2016**, 42, 77.
- [12] J.-S. Jiang, J.-E. Liang, H.-L. Yi, S.-H. Chen, C.-C. Hua, *J. Polym. Res.* **2015**, 22, 144.
- [13] H.-W. Lin, C.-P. Chang, W.-H. Hwu, M.-D. Ger, *J. Mater. Process. Technol.* **2008**, 197, 284.
- [14] C. Xu, N. Willenbacher, *J. Coat. Technol. Res.* **2018**, 15, 1401.
- [15] D. E. Riemer, *Microelectron. Int.* **1989**, 6, 8.
- [16] A. Mette, *New Concepts for Front Side Metallization of Industrial Silicon Solar Cells*, Verl. Dr. Hut, München **2007**.
- [17] W. Li, T. Wu, R. Jiao, B.-P. Zhang, S. Li, Y. Zhou, L. Li, *Colloids Surf. A* **2015**, 466, 132.

- [18] J. Hoornstra, A. W. Weeber, H. H. C. de Moor, W. C. Sinke, presented at *14th European Photovoltaic Solar Energy Conf. (EU PVSEC)*, Barcelona, Spain, July **1997**.
- [19] M. Pospischil, J. Specht, H. Gentscher, M. König, M. Hörteis, C. Mohr, R. Zengerle, F. Clement, D. Biro, presented at *27th European Photovoltaic Solar Energy Conf. (EU PVSEC)*, Frankfurt, Germany, September **2012**.
- [20] R. Faddoul, N. Reverdy-Bruas, J. Bourel, *J. Mater. Sci.: Mater. Electron.* **2012**, 23, 1415.
- [21] Y. Zhou, H. Tong, Y. Liu, S. Yuan, X. Yuan, C. Liu, Y. Zhang, G. Chen, Y. Yang, *J. Mater. Sci.: Mater. Electron.* **2017**, 28, 5548.
- [22] M. M. Hilali, M. M. Al-Jassim, B. To, H. Moutinho, A. Rohatgi, S. Asher, *J. Electrochem. Soc.* **2005**, 152, G742.
- [23] F. Clement, M. Linse, S. Tepner, N. Wengenmeyr, L. Ney, K. Krieg, A. Lorenz, M. Pospischil, S. Bechmann, K. Oehrlé, S. Steckemetz, R. Preu, presented at *36th European Photovoltaic Solar Energy Conf. (EU PVSEC)*, Marseille, France, September **2019**.
- [24] S. Tepner, L. Ney, M. Linse, A. Lorenz, M. Pospischil, K. Masuri, F. Clement, *Prog. Photovoltaics* **2020**, 28, 1054.
- [25] S. Tepner, L. Ney, M. Linse, A. Lorenz, M. Pospischil, K. Masuri, F. Clement, presented at *29th Int. Photovoltaic Science and Engineering Conf. (PVSEC-29)*, Xi'an, China, November **2019**.
- [26] S. Tepner, L. Ney, M. Linse, A. Lorenz, M. Pospischil, F. Clement, *IEEE J. Photovoltaics* **2020**, 10, 319.
- [27] J.-S. Jiang, J.-E. Liang, H.-L. Yi, S.-H. Chen, C.-C. Hua, *Mater. Chem. Phys.* **2016**, 176, 96.
- [28] S. Thibert, J. Jourdan, B. Bechevet, D. Chaussy, N. Reverdy-Bruas, D. Beneventi, *Mater. Sci. Semicond. Process* **2014**, 27, 790.
- [29] S. Tepner, N. Wengenmeyr, M. Linse, A. Lorenz, M. Pospischil, F. Clement, *Adv. Mater. Technol.* **2020**, 5, 2000654.
- [30] C. Xu, M. Fies, N. Willenbacher, *IEEE J. Photovoltaics* **2017**, 7, 129.
- [31] M. Pospischil, J. Specht, M. König, M. Hörteis, C. Mohr, F. Clement, D. Biro, *IEEE J. Photovoltaics* **2014**, 4, 498.
- [32] S. Tepner, N. Wengenmeyr, L. Ney, M. Linse, M. Pospischil, F. Clement, *Sol. Energy Mater. Sol. Cells* **2019**, 200, 109969.
- [33] M. M. Hilali, K. Nakayashiki, C. Khadilkar, R. C. Reedy, A. Rohatgi, A. Shaikh, S. Kim, S. Sridharan, *J. Electrochem. Soc.* **2006**, 153, A5.
- [34] J. D. Fields, M. I. Ahmad, V. L. Pool, J. Yu, D. G. van Campen, P. A. Parilla, M. F. Toney, M. F. van Hest, *Nat. Commun.* **2016**, 7, 11143.
- [35] M. Hörteis, T. Gutberlet, A. Reller, S. W. Glunz, *Adv. Funct. Mater.* **2010**, 20, 476.
- [36] K.-K. Hong, S.-B. Cho, J. S. You, J.-W. Jeong, S.-M. Bea, J.-Y. Huh, *Sol. Energy Mater. Sol. Cells* **2009**, 93, 898.
- [37] D. Quemada, *Rheol. Acta* **1978**, 17, 632.
- [38] K. Gilleo, Screen Print. **1989**, p. 128.
- [39] K.-C. Chiu, in *Proc. Int. Joint Conf. Neural Networks (IJCNN)*, Vol. 2, IEEE, Piscataway, NJ **2003**, pp. 1043–1047.
- [40] M. M. Hilali, in *Proc. IEEE 7th World Conf. Photovoltaic Energy Conversion (WCPEC)*, IEEE, Piscataway, NJ **2018**, pp. 2663–2666.
- [41] R. C. Ball, J. R. Melrose, *Phys. A* **1997**, 247, 444.
- [42] J. F. Brady, G. Bossis, *Annu. Rev. Fluid Mech.* **1988**, 20, 111.
- [43] R. V. More, A. M. Ardekani, *J. Rheol.* **2020**, 64, 67.
- [44] R. V. More, A. M. Ardekani, *J. Rheol.* **2020**, 64, 283.
- [45] R. V. More, A. M. Ardekani, *J. Rheol.* **2020**, 64, 1107.
- [46] R. V. More, A. M. Ardekani, *Phys. Rev. E* **2021**, 103, 062610.
- [47] I. Benedek, *Pressure-Sensitive Adhesives and Applications*, 2nd ed., Marcel-Dekker, Inc., New York, NY **2004**, p. 99.
- [48] S. Pal, R. Saive, presented at *48th IEEE Photovoltaic Specialists Conf. (PVSC)*, June **2021**.
- [49] L. Lu, I. Sevonkaev, A. Kumar, D. V. Goia, *Powder Technol.* **2014**, 261, 87.
- [50] I. Halaciuga, D. V. Goia, *J. Mater. Res.* **2008**, 23, 1776.
- [51] I. Halaciuga, S. LaPlante, D. V. Goia, *J. Colloid Interface Sci.* **2011**, 354, 620.
- [52] D. C.-H. Cheng, *Rheol. Acta* **1986**, 25, 525.
- [53] R. Lapasin, V. Sirtori, D. Casati, *J. Electron. Mater.* **1994**, 23, 525.
- [54] H. Green, R. Weltmann, *Ind. Eng. Chem. Anal. Ed.* **1943**, 15, 201.